Thin Solid Films 760 (2022) 139507

Contents lists available at ScienceDirect

Thin Solid Films

journal homepage: www.elsevier.com/locate/tsf

Ti-Si-B-C-N plasma enhanced chemical vapor deposition nanocomposite coatings for high temperature applications

Alexander Thewes [a,*], Lars Bröcker [a], Emmanuel Tetteh Kofi George [a], Günter Bräuer [a], Michael Paulus [b], Christian Sternemann [b], Hanno Paschke [c], Tristan Brückner [c], Stefan Lechner [d], Sören Müller [d]

[a] Institute for Surface Technology, TU Braunschweig, Field Office Dortmund, Eberhardstr. 12, D-44145 Dortmund, Germany
[b] Fakultät Physik/DELTA, TU Dortmund, Maria-Goeppert-Mayer-Straße 2, D-44227 Dortmund, Germany
[c] Fraunhofer Institute for Surface Engineering and Thin Films IST, IST at DOC, Eberhardstr. 12, D-44145 Dortmund, Germany
[d] Extrusion Research & Development Center, TU Berlin, Gustav-Meyer-Allee 25, Building 17a, Stair 5, D-13355 Berlin, Germany

ARTICLE INFO

Keywords:
Nanocomposite coating
Ti-Si-B-C-N
Plasma enhanced chemical vapor deposition
In-situ X-ray diffraction
Oxidation resistance

ABSTRACT

With increased demands for service lifetime of tools in hot forming applications, e.g. hot extrusion and die-casting, surface modifications of hot working steels are necessary to improve the surface's thermal stability and oxidation resistance. The machining of aluminum and copper is especially challenging, considering its tendency to stick at the tools' surface, which is increasingly impactful at elevated temperatures. Developing Ti-Si-B-C-(N) nanocomposite coatings with plasma-enhanced chemical vapor deposition is a promising approach to overcome these deficiencies, because, with an adequate Si-content, thermal stability and oxidation resistance can be increased by forming a thin, amorphous Si_3N_4 tissue layer between the nanocrystalline grains of the coating. In this study, the influence of nitrogen on the coatings' thermal properties is under investigation for N-content in the range between 0.0 at.-% and 14.6 at.-%. Different oxidation resistance in dependence of the N-content was observed at high temperatures (T = 750-900 °C) *in-situ* by X-ray diffraction in air. The multiphase coatings form compositionally complex nanostructures with an average grain size of ca. 4 to 7 nm. The hardness is strongly affected by nanocomposite structure and residual elements like O and Cl incorporated during coating deposition, whereas the influence of N-content on Ti-Si-B-C-(N) coatings is less significant regarding mechanical properties. Considering the thermal properties, the N-content has been proven to be of central importance. Oxidation was observed in the range between 800 °C and 900 °C, underlining the possible application as protective coating for hot forming tools.

1. Introduction

Tool surfaces in hot forming applications, e.g. aluminum and copper extrusion, are exposed to a harsh tribological environment. The concomitance of thermal load, high forming pressure and adhesive wear from highly reactive forming metals (e.g. Al, Cu) pressed to the tools surface causes severe wear, necessitates the development of adapted wear-resistant coatings. Developing single-phase coatings, which provide high hardness, high toughness, low adhesion to hot metals, corrosive resistance, thermal stability, and oxidation resistance, is demanding [1]. Based on this broad spectrum of requested properties, complex multiphase coatings with nanocomposite structure meet the demands and have attracted much attention in recent years [1–12]. The nanocomposite structure consists of nanocrystalline (nc-) grains embedded in an amorphous (a-) matrix [6,13–18]. To ensure mechanical properties such as a high hardness and toughness, the structure of these coatings is typically composed of 3–10 nm sized grains, which are separated by a 1–3 nm thick a-matrix [4,5]. Due to the Hall-Petch effect, the combination of nc-grains and sharp interfaces between nc-grains and a-matrix enable hardness values that exceed 40 GPa [4,19,20]. For coating systems composed of Ti-(Si,B,C,N), the most commonly detected crystalline phases are nc-TiN, nc-TiC, nc-TiCN, and nc-TiB_2 [1,3,4], whereas the a-matrix can contain a-C, a-BN, a-TiB_2, a-Si_3N_4, a-$TiSi_2$, a-SiC, etc. [4,5,7]. Ternary and quaternary Ti-(B,C)-N coatings yield promising mechanical properties like high hardness and high toughness [12,19,21–23], whereas excellent oxidation resistance is reached by the

* Corresponding author.
E-mail address: alexander.thewes@ist-extern.fraunhofer.de (A. Thewes).

https://doi.org/10.1016/j.tsf.2022.139507
Received 6 December 2021; Received in revised form 19 September 2022; Accepted 19 September 2022
Available online 24 September 2022

use of Ti-Si-N. Consequently, investigations on Ti-Si-(B,C)-N coatings yield similar thermal properties [1,7,9,18,24–29]. However, specific properties of Ti-Si-B-C-N, like phase evolution during coating deposition, hardness, toughness, thermal stability, oxidation resistance, and tribological performance, were not fully investigated, yet [4,29–31]. In this study, the micro- and nanostructure of Ti-Si-B-C-N coatings deposited by plasma-enhanced chemical vapor deposition (PECVD) was investigated via scanning transmission electron microscopy (STEM) and high-resolution transmission electron microscopy (HR-TEM). To complement the optical appearance with information on the a-matrix, Raman spectroscopy was carried out to investigate C phases, e.g. a-C. Hardness, Young's modulus, thickness, and adhesion between coating and substrate were examined. Oxidation resistance of TiN, Ti-B-N, Ti-B-C-N, Ti-Si-B-C, and Ti-Si-B-C-N coatings was studied with *in-situ* X-ray diffraction in air at elevated temperatures.

2. Experimental details

2.1. Coating procedure

Single crystalline Si wafers (ca. $10\times10\times0.2$ mm^3) as well as quenched and tempered (48 HRC) AISI H11 samples of Ø34 mm x 4 mm size were coated in a pulsed direct current PECVD PN 100/150 device (Ruebig GmbH & Co. KG, Austria; see Appendix A), as described elsewhere [29]. The samples were ultrasonically cleaned for 15 min in isopropanol, before they were installed in the vacuum chamber for processing. Pretreatments in vacuum, such as 30 min sputtering for plasma etching, and 30 min plasma nitriding, were carried out prior to coating deposition. Plasma nitriding was carried out in an atmosphere with low $N_2/(N_2+H_2)$ ratio of 5% and additional Ar for plasma support. Further parameters are a working pressure of p = 240 Pa, an applied bias voltage of U = -480 V and a substrate temperature of T = 530 °C. These parameters were utilized to increase the adhesion between the steel substrate and hard coating [32].

The Ti-Si-B-C-(N) coatings were subsequently coated with a TiN adhesion layer, a graded layer to grant a smooth transition from TiN to the Ti-Si-B-C-(N) and a top layer. The top layer itself was produced with fixed coating parameters, e.g. precursor mass flows. They were deposited using a gaseous mixture of $TiCl_4$, BCl_3, N_2 (except for the Ti-Si-B-C coating), and $Si(CH_3)_4$ (tetramethylsilane, TMS). In addition, small quantities of Ar were utilized to support a stable glow discharge, and H_2 was added to reduce the chlorine of $TiCl_4$ and BCl_3 molecules. The coatings were deposited at p = 200 Pa, U = −480 to −580 V, duty cycle of D = 0.33, and at sample temperature of T = 530 °C. The N_2 flow was varied from 0 to 667 sccm in 167 sccm steps to extrapolate the influence of nitrogen on the formation of Ti-Si-B-C-(N), whereas every other coating parameter was kept constant. Aside from this field study, a coating was deposited with a N_2 flow of 167 sccm and a TMS flow reduced from 67 to 33 sccm. TiN, Ti-B-N, and Ti-B-C-N were deposited for comparison with Ti-Si-B-C-(N) coatings with the same deposition device and under similar conditions (plasma, deposition temperature, pressure), but under use of fewer (BCl_3, TMS) or different (CH_4) precursors.

2.2. Coating characterization

The chemical composition was determined by means of electron probe microanalysis (EPMA) using an electron probe microanalyzer SX100 device (Cameca, France). The excitation energy was 10 keV. Coatings' thicknesses were determined via ball cratering method, using a kaloMAX NT device (BAQ GmbH, Germany), as described by Leroy et al. [33]. The microstructure was analyzed using a Cross-Beam 340 (Carl Zeiss AG, Germany) performing STEM with an excitation energy of 30 kV. HR-TEM images for analysis of nanostructure were taken using a JEOL JEM 2200fs device (JEOL, Japan). The excitation energy was set to 200 kV. The adhesive behavior of the coatings on quenched and tempered AISI H11 was evaluated by Rockwell C Indentation tests according to DIN 4856:2018–02 [34]. To increase reliability, three indentations per coating were performed. The hardness and Young's modulus were measured with a Fisherscope using Berkovich indentation mode [35]. X-ray diffraction was carried out at beamline BL9 of the synchrotron radiation source DELTA (TU Dortmund University, Germany [36]) at room temperature (RT; ~25 °C) and *in-situ* with thermal loads of 750 °C, 800 °C, 850 °C, 875 °C and 900 °C, respectively. The measurements were conducted directly after reaching the temperature level and each took approximately 15 min. The photon energy was set to E_0 = 13 keV and a beam size with a width of 1.5 mm and height of 0.2 mm was used. Due to the small thickness of the deposited coatings (1.6 to 4.5 μm), the angle of incidence was set to 1° To avoid strong heat convection through air, a small graphite dome was utilized to isolate the air from the surroundings, as well as to ensure a constant sample temperature. A PILATUS 100 K detector was used for the X-ray diffraction measurements. Grain sizes of nc-grains were calculated via the Scherrer equation at RT with a geometrical factor K = 0.9. The TiC grainsize was determined at scattering angles of ~25.4° at RT, whereas TiN grainsize was determined at scattering angles of ~25.6° and ~36.6° Note that for TiC, there is no error bar given, as it is a single data point. For Raman studies, a DXR2 Raman Microscope (Thermo Fisher Scientific, Germany) with a laser wavelength of 532 nm, a laser power of 6 W and a 50 μm slit was used with 300 exposures of 5 s length for every spectrum. The experiments were performed on the same coating, once as-deposited and once after 30 min annealing in air at 900 °C.

3. Results and discussion

The chemical compositions of the deposited Ti-Si-B-C-(N) coatings are listed in Table 1. As the coating processes were carried out with varying N_2 flow rates, which changes the composition of the atmosphere in the deposition chamber, different chemical compositions with N-contents between 0.0 to 14.6 at.-% were obtained. C-contents were in the range of 28.5 to 37.5 at.-%, which is comparable to results published by Ma et al. [7]. They found C-contents of 25.3, 29.3, and 38.6 at.-% in quaternary Ti-Si-C-N nanocomposites with low coefficient of friction. 25.7 to 32.0 at.-% Ti was found, forming nc-Ti(C,N). The different proportion of N-content influences phase formation of nc-Ti(C)N and a-Si_3N_4, the phase that has been identified as the most important compound for thermal stability and oxidation resistance in Ti-Si-N nanocomposites [9,26,37,38]. Residuals of O and Cl were detected in the range of 1.4 to 3.4 at.-% and 0.7 to 3.5 at.-%, respectively. These residuals tend to have a major impact on the hardness and a minor impact on the oxidation resistance [11,38,39].

The microstructure of $TiSiBCN_{8.7}$ is shown in Fig. 1. The TiN adhesion layer and adjected regions of the graded interlayer show a dense but dendritic appearing structure, as seen in the close-up. In contrast, the rest of the interlayer and the top layer show a structure that appears homogenous on the microscale. On the nanoscale, a fine-grained structure with grains of different orientation can be observed (compare Fig. 2a; orientations marked with red lines). The size of nc-grains was measured optically (see Fig. 2 b) to 4 to 6 nm and fits into the expected 3 to 10 nm range. However, it should be noted that this method provides only a rough estimation on the grain size.

The HRC indentations of the coatings are given in Fig. 3a – f. All pictures show concentric rings around the indentation in the center. These are often accompanied by fine radial cracks in between the concentric rings. Here, the important part for evaluation of adhesion is the area directly surrounding the indentation crater (in between the two red rings in each picture). In this region, no significant areas of spallation of coating could be detected. It has to be noted, that in Fig. 3e the radial cracks around the crater are close packed and wide. Additionally, spallation between two concentric rings can be detected in this case (encircled in blue, dotted line on the left-hand side of the red rings). Coatings 'a' TiSiBC, 'b' $TiSiBCN_{4.4}$, 'c' $TiSiBCN_{8.7}$, and 'f' $TiSiBCN_{9.4}$ are

Table 1
Chemical composition [at.-%] in dependence of N_2 and TMS flow [sccm] determined by EPMA analysis.

Coating	N_2 flow [sccm]	TMS flow [sccm]	Coating elements [at.-%]					Residuals [at.-%]	
			Ti	Si	B	C	N	O	Cl
TiSiBC	**0**	67	25.7	12.4	20.1	37.5	**0.0**	2.2	2.1
$TiSiBCN_{4.4}$	**167**	67	32.0	9.3	17.5	33.0	**4.4**	1.4	2.3
$TiSiBCN_{9.4}$	**167**	**33**	33.6	8.4	13.3	30.1	**9.4**	1.5	0.7
$TiSiBCN_{8.7}$	**333**	67	30.0	9.6	15.5	32.1	**8.7**	1.5	2.7
$TiSiBCN_{12.9}$	**500**	67	30.0	9.1	14.0	29.2	**12.9**	1.8	3.0
$TiSiBCN_{14,6}$	**667**	67	26.7	9.5	13.8	28.5	**14.6**	3.4	3.5

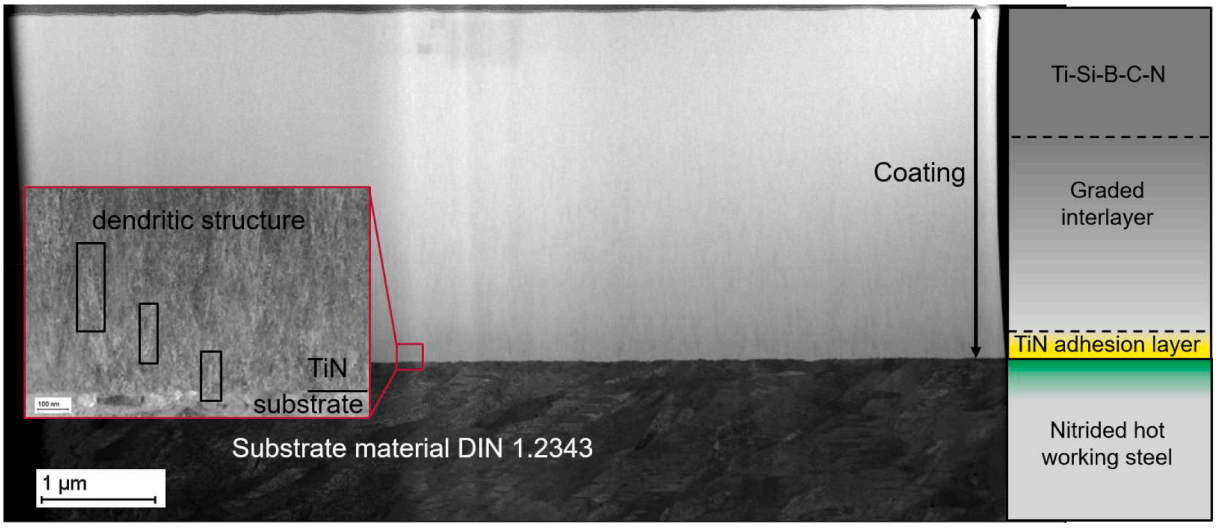

Fig. 1. STEM picture of $TiSiBCN_{8.7}$ with close-up view of the substrate-coating interface and schematic build on the right-hand side.

HF2, whereas 'd' $TiSiBCN_{12.9}$ and 'e' $TiSiBCN_{14.6}$ are HF3.

The mechanical properties are summarized in Table 2. Here, the coatings show hardness values in the range of 20.4 to 39.3 GPa. However, nanocomposites are known for hardness reaching 40 GPa or more [3,10]. One possible explanation is, that the volumetric ratio of the a-matrix is outside of the range of 15% to 25% of the coating, where according to Patscheider et al. a hardness maximum in nanocomposite coatings is reached [40]. Another possible explanation is the proportion of O and Cl found in the samples. $TiSiBCN_{9.4}$ contains the lowest amount of O (1.5 at.-%) and Cl (0.7 at.-%) and offers a hardness of 39 GPa. Vepřek et al. [38] state in their review, that residuals of O + Cl have a massive influence on the coatings' properties, especially the hardness. Fig. 4 offers the hardness values with regard to the amount of O and Cl in the coating. The gray box in Fig. 4 marks the area where 'superhardness' is expected. For Ti-Si-B-C-N coatings, the hardness values decrease with increasing O and Cl. The Ti-Si-B-C coating appears to be different from Ti-Si-B-C-N coatings, but fits the bigger picture. In summary, the decrease in hardness is most likely a result of chemical effects of O and Cl within the coatings' structure, rather than the nanocomposite build-up itself. Thus, the differences in hardness values observed in this work probably derive primarily from O and Cl and neither from deposition conditions like temperature or bias voltage nor from differences in C- and N-content or nanocomposite structure. Only in case of a significant increase (quasi-amorphous coating) or decrease (almost fully crystalline coating) in volumetric ratio of the a-matrix, the hardness will be reduced below 40 GPa independent of O and Cl, as described by Patscheider et al. [40]. The assumption of the impact of O and Cl is supported by grain sizes in a close range of 4.1 to 6.5 nm (see Table 3 and Fig. 2b) that are densely packed (see Fig. 2a). Thus, neither the a-matrix is too thin nor the grains are too large (Hall-Petch effect) or too small (inverse Hall-Petch effect) to yield hardness values > 40 GPa [41].

The oxidation resistance of Ti-Si-B-C-N coatings is significantly different from those of TiN (50 at.-% Ti, 50 at.-% N), Ti-B-N (ca. 40 at.-% Ti, 46 at.-% B, 14 at.-% N), and Ti-B-C-N (49 at.-% Ti, 16 at.-% B, 3 at.-% C, 32 at.-% N), which is shown in Fig. 5. The composition of Ti-B-N is only given by an estimation, because the composition was only measured for a coating in a similar Ti-B-N coating process in the same deposition device. The four different patterns were each measured *in-situ* at a temperature of 750 °C in air. The patterns of TiN, Ti-B-N, and Ti-B-C-N show strong TiO_2 Bragg reflections, indicating the oxidation of the surface near zone. TiN is known for low oxidation resistance, tending to transform into TiO_2 at 500 °C [42]. In this study, rutile TiO_2 is observed, but no anatase TiO_2. For Ti-B-N coatings, Kiryukhantsev-Korneev et al. [8] report a beginning of oxidation at around 600 °C. In a previous work, the authors found the Ti-B-N coating to be intact at 500 °C and heavily oxidized at 750 °C [29]. Here, the coatings show a weakly pronounced TiN Bragg reflection and several reflexes of rutile and anatase. An extensive study by Chen et al. [43] on the oxidation resistance of Ti-B-C-N coatings lead to the conclusion, that these coatings are stable up to 600-700 °C, depending on their chemical composition (C-contents of 48.8 at.-% and 54.2 at.-% proved unbeneficial for thermal properties). The presented Ti-B-C-N coating showed a strong Ti(C,N) (200) reflex, six rutile TiO_2 reflexes and one weak anatase TiO_2 reflex. To sum up, the results for TiN, Ti-B-N, and Ti-B-C-N shown in Fig. 5 match with those derived from literature and rutile is the dominating TiO_2 phase in those coating systems after oxidation. The X-ray diffraction pattern of Ti-Si-B-C-N in Fig. 5 does not show any sign of TiO_2 phases, leading to the conclusion that the starting point for oxidation has not been reached. The same behavior was observed for different N-contents at 750 °C ($TiSiBCN_{4.4}$ to $TiSiBCN_{14.6}$). In conclusion, Si is the element that enables high oxidation resistance. A possible explanation for this behavior is provided by a consideration of Ti-Si-N nanocomposite coatings. Here, extensive research was carried out and an a-Si_3N_4 containing matrix was identified to be the origin of the observed temperature stability [9,26,

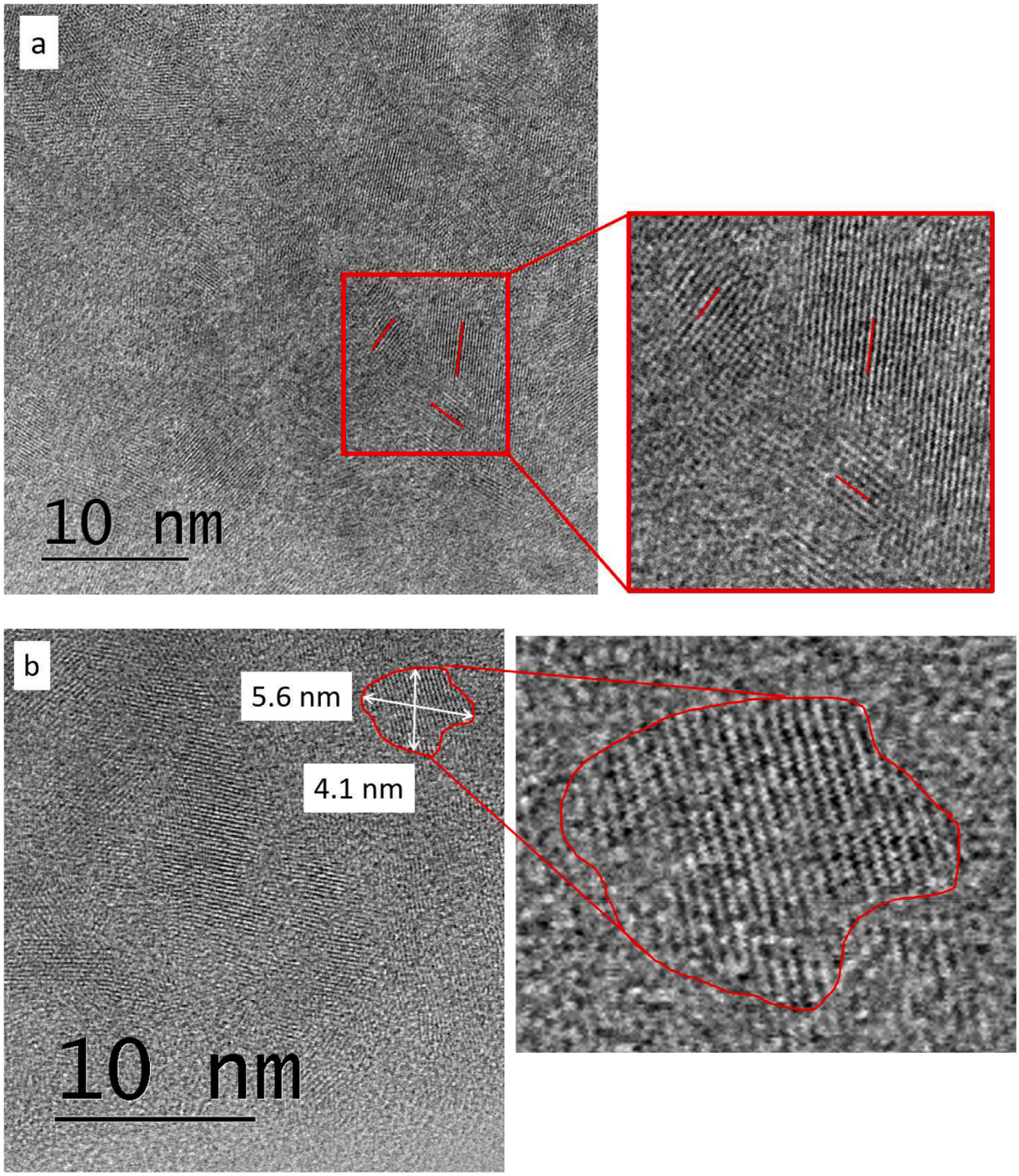

Fig. 2. HR-TEM pictures of the top layer of $TiSiBCN_{8.7}$. (a) Overview and close-up view of different grains. The red lines indicate grain orientation. (b) Approximation of grain size.

38]. Nevertheless, Mahato et al. [18] deposited Ti-Si-B-C, a coating system that is unable to develop Si_3N_4 due to its lack of N, also observing a high oxidation resistance of up to 800 to 1.000 °C. In order to obtain further information on the underlying processes, temperature dependent diffraction experiments were performed on a coating that did not contain nitrogen. *In-situ* X-ray diffraction of a Ti-Si-B-C coating with patterns measured at multiple temperature levels was carried out (see Fig. 6). At RT, characteristic reflexes of the graphite dome, which is part of the heating cell, and of TiC are found. The TiC (200) and (220) reflections are identified at scattering angles of ~25.4° and ~36.5°, respectively [3]. Starting from RT up to 900 °C, the reflexes reduce slightly in intensity with increasing temperature. Still, the TiC (200) peak is stronger pronounced than the other peaks, regardless of temperature level. Oxidation starts at 800 °C and accelerates with increasing temperature as can be seen by rutile TiO_2 reflexes (compare Fig. 6). Anatase TiO_2 was not observed. Underneath an oxide layer, the as-deposited coating appears to be intact, as evidenced by the strongly pronounced TiC (200) reflex. To conclude, these results are in agreement with Mahato et al. [18]. Mahato et al. propose that the Si and Ti incorporated in the coating oxidize to SiO_2 and TiO_2, respectively, which in turn build a passivating oxide layer on the surface. They observed the formation of SiO_2 phases in their X-ray diffraction measurement. However, in this work, no characteristic reflection of nc-SiO_2 was detected at scattering angles of 17° or 18° In summary, the formation of a

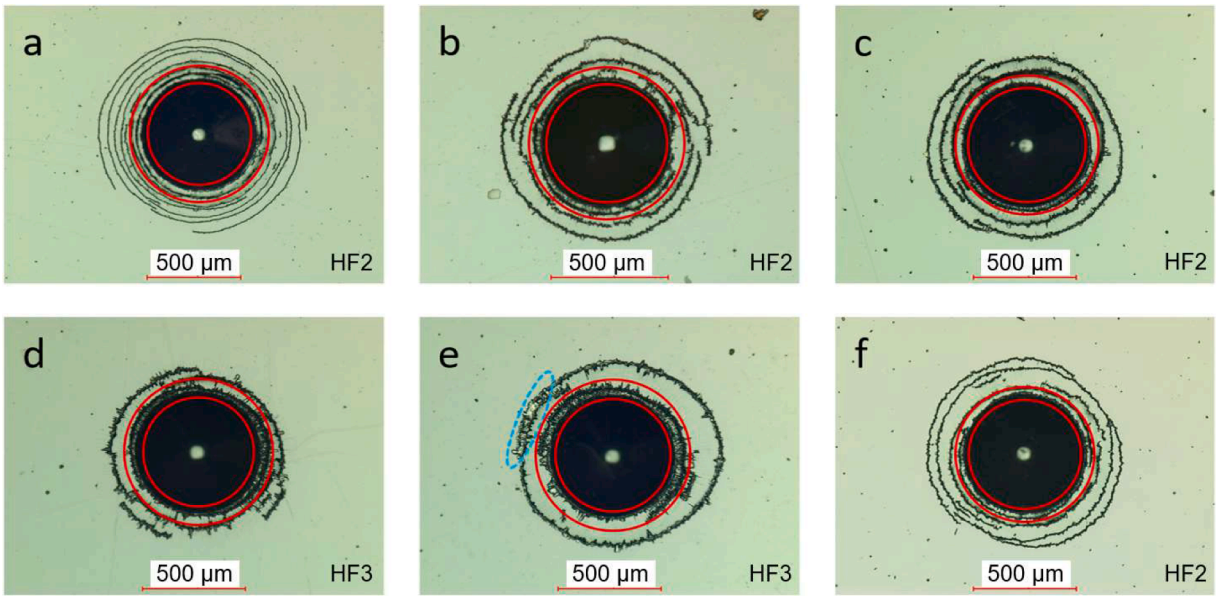

Fig. 3. HRC indentations into a) TiSiBC, b) $TiSiBCN_{4.4}$, c) $TiSiBCN_{8.7}$, d) $TiSiBCN_{12.9}$, e) $TiSiBCN_{14.6}$, and f) $TiSiBCN_{9.4}$.

Table 2
Mechanical properties of Ti-Si-B-C-(N) determined by nanoindentation (hardness, Young's modulus and fracture toughness) and ball cratering method (thickness).

Coating	Hardness [GPa]	Young's modulus [GPa]	Fracture toughness H/E [ ]	Thickness [µm]
TiSiBC	29.2 ± 2.4	218.1 ± 7.3	0.134 ± 0.016	1.7 ± 0.2
$TiSiBCN_{4.4}$	31.3 ± 1.6	250.9 ± 7.4	0.125 ± 0.010	3.4 ± 0.4
$TiSiBCN_{8.7}$	24.9 ± 1.2	212.4 ± 6.1	0.117 ± 0.010	3.6 ± 0.5
$TiSiBCN_{9.4}$	39.3 ± 2.7	294.0 ± 11.2	0.134 ± 0.015	3.0 ± 0.3
$TiSiBCN_{12.9}$	23.3 ± 1.4	202.5 ± 6.6	0.115 ± 0.011	4.0 ± 0.5
$TiSiBCN_{14.6}$	20.4 ± 0.8	181.2 ± 3.4	0.113 ± 0.007	4.4 ± 0.5

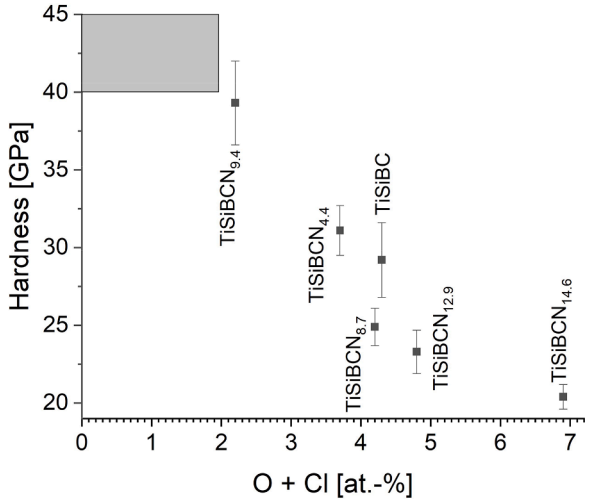

Fig. 4. Hardness in correlation to O and Cl residuals in the coatings with varying N-content.

nc-SiO_2/nc-TiO_2 passive layer was not observed within this work. This does not exclude the possibility of a-SiO_2/nc-TiO_2 formation. However, Mahato et al. deposited coatings with 19.2 at.-% Ti and 19.4 at.-% Si, whereas here coatings with 25.7 at.-% Ti and 12.4 at.-% Si are discussed. With more Si and less Ti, formation of nc-SiO_2 during oxidation is more likely to occur. Furthermore, the X-ray diffraction spectra are mainly sensitive to crystalline SiO_2 phases, whereas amorphous phases are less clearly imaged. Finally, the influence of N on the temperature behavior of Ti-Si-B-C-N coatings is discussed. Therefore, the N-content was varied and *in-situ* X-ray diffraction measurements were carried out at multiple temperature levels. Due to the extensive data resulting from 20 X-ray diffraction patterns, Fig. 7 only shows the patterns of TiSiBC, $TiSiBCN_{4.4}$, $TiSiBCN_{8.7}$, $TiSiBCN_{12.9}$, and $TiSiBCN_{14.6}$ at 875 °C, because the differences are the most significant at this temperature level. For TiSiBC, the as deposited TiC (200) reflex at a scattering angle of 25.4° offers the

Table 3
Grain sizes calculated with the Scherrer equation.

Coating	nc-TiC [nm]	nc-TiN [nm]
TiSiBC	5.0	–
$TiSiBCN_{4.4}$	–	6.5 ± 0.3
$TiSiBCN_{8.7}$	–	6.2 ± 0.6
$TiSiBCN_{12.9}$	–	5.8 ± 0.2
$TiSiBCN_{14.6}$	–	5.3 ± 0.3

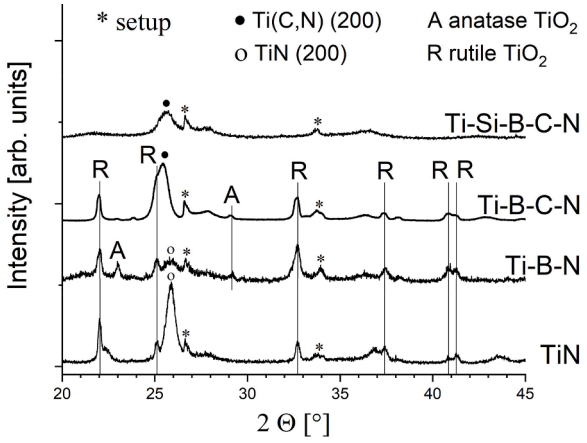

Fig. 5. *In-situ* X-ray diffraction patterns of TiN, Ti-B-N, Ti-B-C-N, and Ti-Si-B-C-N coatings at 750 °C. Vertical lines mark rutile (R) and anatase (A) TiO_2 reflexes.

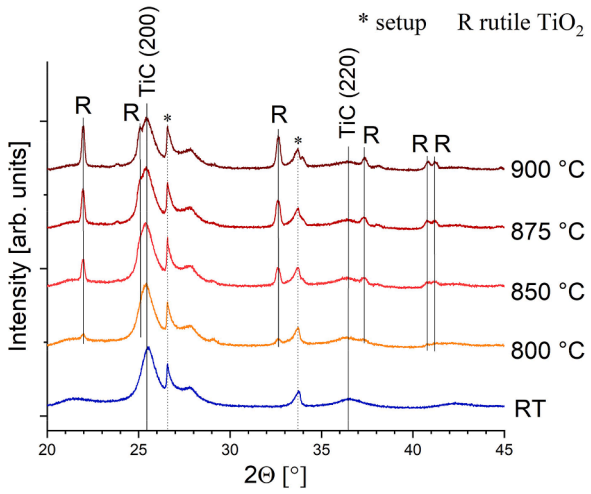

Fig. 6. *In-situ* X-ray diffraction patterns at room temperature, 800 °C, 850 °C, 875 °C, and 900 °C of TiSiBC (chemical composition see table 1).

maximum peak intensity. The other coating systems contain additional nitrogen and are able to form nc-TiN in addition to nc-TiC. These phases show similar lattice structures, resulting in overlapping (200) Bragg reflections. This has been observed by many researchers who carried out investigations on Ti-C-N and Ti-B-C-N coatings [21,44]. In result, these reflexes are often marked with Ti(C,N), because a definite assignment to one or the other is impossible. In this work, these reflexes of (200), (220), and (311) are found at scattering angles of ~25.4°, ~36.6°, and ~43.0°, respectively. It is evident, that, with increasing N-content, the formation of rutile and anatase TiO_2 phases are weaker pronounced. Thus, more N leads to higher oxidation resistance and presumably the formation of a-Si_3N_4 phase. A closer look at Fig. 7 shows, that even at a very high temperature of 875 °C, protection against oxidation of the coating is given, at least at high N-contents. Thus, the X-ray diffraction measurements on the coatings with 12.9 at.-% and 14.6 at.-% N show significantly lower TiO_2 signals than the coatings with lower N-content. As the molar volume of TiO_2 is bigger than that of TiN, crack opening of the adjacent SiO_2 passivation layer occurs when TiO_2 grains form [40]. To sum up, the surface-near zone oxidizes, but Ti(C,N) indicates an intact, as-deposited zone underneath and slow oxidation rates. The Raman spectra in Fig. 8 offer additional information on the a-matrix. The as-deposited $TiSiBCN_{8.7}$ coating contained a-C, as can be identified in the D Band (1355 cm^{-1}) and G Band (1585 cm^{-1}) responses. Combined with the results from HR-TEM analytics, the existence of nc-grains and a-matrix was proven in this study. Furthermore, annealing the sample in air for 30 min at 900 °C showed that the a-C oxidizes, as no peaks at D Band or G Band can be identified afterwards. The a-C is not protected from oxidation by a passivation layer of e.g. TiO_2 or SiO_2, so that probably a chemical reaction with O_2 from air turns a-C into CO_2, which desorbs form the coating.

4. Conclusions

Duplex processing in form of nitriding and PECVD coating deposition was carried out to form thermally stable Ti-Si-B-C-(N) nanocomposites on hot working steel substrates. STEM, HR-TEM, X-ray diffraction, and Raman spectroscopy proved nanocrystalline grains as well as an a-matrix that contains a-C. HRC indentations proved good adhesion between hot working steel and nanocomposite coating due to plasma nitriding and an adhesive TiN interlayer. The oxidation resistance of thin films was investigated by means of *in-situ* X-ray diffraction at elevated temperatures. The Si-free coatings TiN, Ti-B-N, and Ti-B-C-N oxidized below 750 °C, whereas Ti-Si-B-C—N showed no significant differences to the as-deposited state. Increasing N-content from 0 to 14.6 at.-% in Ti-Si-B-C-(N) led to higher oxidation resistance in the range of 800 °C to 900 °C, presumably resulting from an increase in a-Si_3N_4 phase. For use in high temperature wear applications, Ti-Si-B-C-N should contain at least 10 at.-% N. The deposition of a 39.3 GPa hard Ti-Si-B-C—N coating is an indicator for possible superhardness (> 40 GPa) in these coatings and

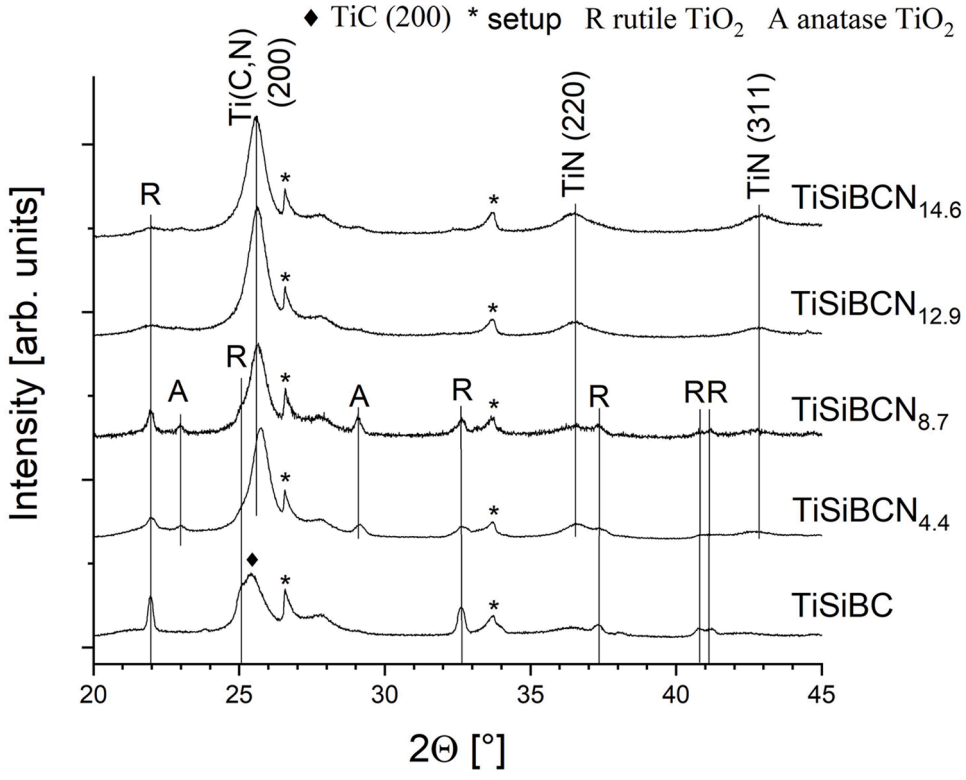

Fig. 7. *In-situ* X-ray diffraction patterns of Ti-Si-B-C and Ti-Si-B-C-N (chemical composition see table 1) coatings at 875 °C.

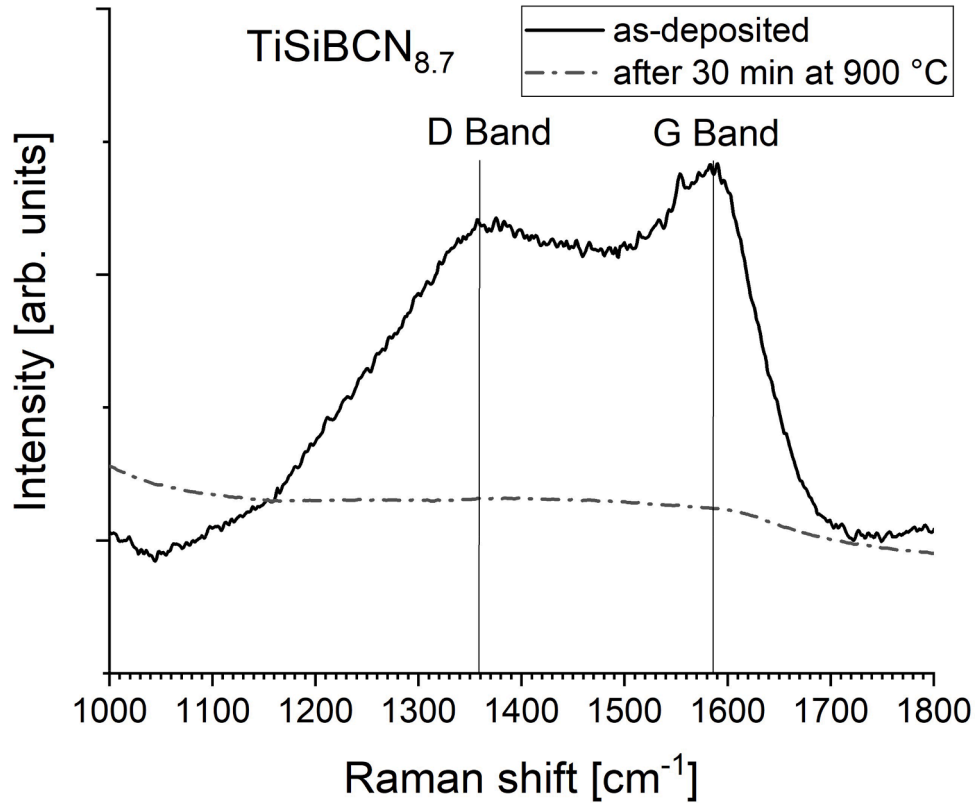

Fig. 8. Raman pattern of as-deposited and air-annealed (30 min, 900 °C) coating $TiSiBCN_{8.7}$.

was achieved in an industrial sized deposition plant (Ø1,000 mm x 1800 mm). In combination with the thermal properties, these coatings seem promising for tools in hot forming applications. Further work will include investigations of the nanocomposite structure (X-ray photoelectron spectroscopy) measurements to prove a-Si_3N_4), the coating's adhesion, and the mechanical properties.

CRediT authorship contribution statement

Alexander Thewes: . **Lars Bröcker:** Data curation, Investigation. **Emmanuel Tetteh Kofi George:** Writing – review & editing, Data curation, Investigation. **Günter Bräuer:** Supervision, Writing – review & editing. **Michael Paulus:** Data curation, Investigation, Writing – review & editing. **Christian Sternemann:** Data curation, Investigation, Writing – review & editing. **Hanno Paschke:** Writing – review & editing, Funding acquisition. **Tristan Brückner:** Writing – review & editing. **Stefan Lechner:** Writing – review & editing. **Sören Müller:** Writing – review & editing, Funding acquisition.

Declaration of Competing Interest

The authors declare that they have no known competing financial interests or personal relationships that could have appeared to influence the work reported in this paper.

Data availability

Data will be made available on request.

Acknowledgement

The authors thank the DELTA machine group for providing the synchrotron radiation at beamline BL9. In addition, the contributions of Dr. Petersen and Mrs. Steinberg, Fraunhofer Institute for Surface Engineering and Thin Films IST, in form of EPMA measurements and STEM analysis, are highly appreciated. Special thanks to Dr. Heidelmann and Mr. Nguyen, Interdisciplinary Center for Analytics on the Nanoscale (ICAN) at University of Duisburg-Essen, for HR-TEM analysis to prove the nanocomposite structure of the coating. The research project (No. 19862 N) of the research association "Stifterverband Metalle e.V." has been supported financially within the program of the "Industrielle Gemeinschaftsforschung (IGF)" by the "Bundesministerium fuer Wirtschaft und Technologie" via the AiF. We are thankful for the assistance given.

Appendix A: Industrial-sized PECVD deposition device (Ruebig GmbH & Co. KG, Austria)

References

[1] S.K. Mishra, P. Mahato, B. Mahato, L.C. Pathak, Thermal stability and effect of substrate temperature of TiSiBC hard nanocomposite coatings on microstructure, mechanical, thermal behaviour deposited by magnetron sputtering, Appl Surf Sci 266 (2013) 209–213.

[2] M.A. Meyers, A. Mishra, D.J. Benson, Mechanical properties of nanocrystalline materials, Prog Mater Sci 51 (2006) 427–556.

[3] C. Mitterer, P.H. Mayrhofer, M. Beschliesser, s, Microstructure and properties of nanocomposite Ti-B-N and Ti-B-C coating, Surface and Coatings Technology (1999) 405–411.

[4] I.W. Park, B. Mishra, K.H. Kim, J.J. Moore, Multifunctional Ti-Si-B-C-N Tribological Nanocomposite Coatings for Aerospace Applications, MSF 539-543 (2007) 173–180.

[5] E. Thangavel, S. Lee, K.-.S. Nam, J.-.K. Kim, D.-.G. Kim, Synthesis and characterization of Ti–Si–C–N nanocomposite coatings prepared by a filtered vacuum arc method, Appl Surf Sci 265 (2013) 60–65.

[6] J. Lin, R. Wei, D.C. Bitsis, P.M. Lee, Development and evaluation of low friction TiSiCN nanocomposite coatings for piston ring applications, Surface and Coatings Technology 298 (2016) 121–131.

[7] S.L. Ma, D.Y. Ma, Y. Guo, B. Xu, G.Z. Wu, K.W. Xu, P.K. Chu, Synthesis and characterization of super hard, self-lubricating Ti–Si–C–N nanocomposite coatings, Acta Mater 55 (2007) 6350–6355.

[8] P.V. Kiryukhantsev-Korneev, D.V. Shtansky, M.I. Petrzhik, E.A. Levashov, B. N. Mavrin, Thermal stability and oxidation resistance of Ti–B–N, Ti–Cr–B–N, Ti–Si–B–N and Ti–Al–Si–B–N films, Surface and Coatings Technology 201 (2007) 6143–6147.

[9] D. Pilloud, J.F. Pierson, M.C. Marco de Lucas, A. Cavaleiro, Study of the structural changes induced by air oxidation in Ti–Si–N hard coatings, Surface and Coatings Technology 202 (2008) 2413–2417.

[10] J. Marashi, E. Yakushina, P. Xirouchakis, R. Zante, J. Foster, An evaluation of H13 tool steel deformation in hot forging conditions, Journal of Materials Processing Technology 246 (2017) 276–284.

[11] J. Procházka, P. Karvánková, M.G.J. Vepřek-Heijman, S. Vepřek, Conditions required for achieving superhardness of ≥ in nc-TiN/a-Si3N4 nanocomposites, Materials Science and Engineering: A 45 GPa 384 (2004) 102–116.

[12] H. Paschke, M. Stueber, C. Ziebert, M. Bistron, P. Mayrhofer, Composition, microstructure and mechanical properties of boron containing multilayer coatings for hot forming tools, Surface and Coatings Technology 205 (2011) 24–28.

[13] P. Mahato, G. Nyati, R.J. Singh, S.K. Mishra, Nanocomposite TiSiBC Hard Coatings with High Resistance to Wear, Fracture and Scratching, J. of Materi Eng and Perform 25 (2016) 3774–3782.

[14] Q.H. Luo, Y.H. Lu, Microstructure and mechanical properties of reactive magnetron sputtered Ti–B–C–N nanocomposite coatings, Appl Surf Sci 258 (2011) 1021–1026.

[15] J. Houska, J. Kohout, P. Mares, R. Cerstvy, J. Vlcek, Dependence of structure and properties of hard nanocrystalline conductive films MBCN (M = Ti, Zr, Hf) on the choice of metal element, Thin Solid Films 586 (2015) 22–27.

[16] M. Diserens, J. Patscheider, F. Lévy, Improving the properties of titanium nitride by incorporation of silicon, Surf Coat Technol (1998) 241–246.

[17] S. Vepřek, S. Reiprich, L. Shizhi, Superhard nanocrystalline composite materials: the TiN/Si 3 N 4 system, Appl. Phys. Lett. 66 (1995) 2640–2642.

[18] P. Mahato, R.J. Singh, S.K. Mishra, Nanocomposite Ti–Si–B–C hard coatings deposited by magnetron sputtering: oxidation and mechanical behaviour with temperature and duration of oxidation, Surf Coat Technol (2016) 230–240.

[19] W. Gissler, Structure and properties of Ti-B-N Coatings, Surface and Coatings Technology (1994) 556–563.

[20] C.E. Carlton, P.J. Ferreira, What is behind the inverse Hall–Petch effect in nanocrystalline materials? Acta Mater 55 (2007) 3749–3756.

[21] K.H. Kim, J.T. Ok, S. Abraham, Y.-.R. Cho, I.-.W. Park, J.J. Moore, Syntheses and mechanical properties of Ti–B–C–N coatings by a plasma-enhanced chemical vapor deposition, Surface and Coatings Technology 201 (2006) 4185–4189.

[22] P. Karvankova, Azinovic Vepřek-Heijmann, D.S.. V.epřek, Properties of superhard nc-TiN/a-BN and nc-TiN/a-BN/a-TiB2 nanocomposite coatings prepared by plasma induced chemical vapor deposition, Surface and Coatings Technology (2006) 2978–2989.

[23] P.H. Mayrhofer, M. Stoiber, Thermal stability of superhard Ti–B–N coatings, Surface and Coatings Technology 201 (2007) 6148–6153.

[24] S. Ma, J. Procházka, P. Karvánková, Q. Ma, X. Niu, X. Wang, D. Ma, K. Xu, S. Vepřek, Comparative study of the tribological behaviour of superhard nanocomposite coatings nc-TiN/a-Si3N4 with TiN, Surface and Coatings Technology 194 (2005) 143–148.

[25] A. Niederhofer, T. Bolom, P. Nesladek, K. Moto, C. Eggs, D.S. Patil, S. Vepřek, The role of percolation threshold for the control of the hardness and thermal stability of

super- and ultrahard nanocomposites, Surface and Coatings Technology 146-147 (2001) 183–188.
[26] P. Steyer, D. Pilloud, J.F. Pierson, J.-.P. Millet, M. Charnay, B. Stauder, P. Jacquot, Oxidation resistance improvement of arc-evaporated TiN hard coatings by silicon addition, Surface and Coatings Technology 201 (2006) 4158–4162.
[27] M. Pleva, B. Grančič, M. Mikula, M. Truchlý, T. Roch, L. Satrapinskyy, M. Gregor, P. Ďurina, V. Girman, P. Švec, A. Plecenik, P. Kúš, Thermal stability of amorphous Ti-B-Si-N coatings with variable Si/B concentration ratio, Surface and Coatings Technology 333 (2018) 52–60.
[28] M. Abedi, A. Abdollah-zadeh, M. Bestetti, A. Vicenzo, A. Serafini, F. Movassagh-Alanagh, The effects of phase transformation on the structure and mechanical properties of TiSiCN nanocomposite coatings deposited by PECVD method, Appl Surf Sci 444 (2018) 377–386.
[29] A. Nienhaus, G. Braeuer, H. Paschke, D. Stangier, W. Tillmann, M. Paulus, C. Sternemann, Nanocomposite PECVD multiphase coatings for wear reduction under thermal load conditions, in: Proceedings 3. Niedersaechsisches Symposium Materialtechnik, 2019, pp. 539–543, https://doi.org/10.21268/20190320-4.
[30] P. Mahato, S.K. Mishra, N.C. Murmu, P. Banerjee, Enhancement of the Mechanical and Tribological Performance of Stainless Steel 304 by Ti-based Nanocomposite Coatings Deposited by PVD Method, Triboindia (2018), https://doi.org/10.2139/ssrn.3313493.
[31] J. Houska, P. Mares, V. Simova, S. Zuzjakova, R. Cerstvy, J. Vlcek, Dependence of characteristics of MSiBCN (M=Ti, Zr, Hf) on the choice of metal element: experimental and ab-initio study, Thin Solid Films (2016) 359–365.
[32] B.S. Yilbas, S.M. Nizam, Wear behavior of TiN coated AISI H11 and AISI M7 twist drills prior to plasma nitriding, Journal of Materials Processing Technology (2000) 352–358.
[33] C. Leroy, K.I. Schiffmann, K. van Acker, J. von Stebut, Ball cratering an efficient tool for 3 body microabrasion of coated systems, Surface and Coatings Technology (2005), 153156.
[34] German Institute for Standardization, DIN 4856:2018-02, Carbon-based films and Other Hard Coatings - Rockwell penetration Test to Evaluate Adhesion, 2018.
[35] M. Lichinchi, C. Lenardi, J. Haupt, R. Vitali, Simulation of Berkovich nanoindentation experiments on thin films using finite element method, Thin Solid Films (1998) 240–248.
[36] C. Krywka, M. Paulus, C. Sternemann, M. Volmer, A. Remhof, G. Nowak, A. Nefedov, B. Pöter, M. Spiegel, M. Tolan, The new diffractometer for surface X-ray diffraction at beamline BL9 of DELTA, J. Synchrotron Radiat. 13 (2006) 8–13.
[37] X. Sun, J.S. Reid, E. Kolawa, M.-.A. Nicolet, Reactively sputtered Ti-Si-N films I. Physical properties, J Appl Phys 81 (1997) 656–663.
[38] S. Vepřek, M.G.J. Vepřek-Heijman, P. Karvankova, J. Prochazka, Different approaches to superhard coatings and nanocomposites, Thin Solid Films 476 (2005) 1–29.
[39] S. Vepřek, H.-.D. Männling, P. Karvankova, J. Prochazka, The issue of the reproducibility of deposition of superhard nanocomposites with hardness of $\geq$50 GPa, Surface and Coatings Technology 200 (2006) 3876–3885.
[40] J. Patscheider, T. Zehnder, M. Diserens, Structure-performance relations in nanocomposite coatings, Surface and Coatings Technology 146-147 (2001) 201–208.
[41] S. Zhang, D. Sun, Y. Fu, H. Du, Effect of sputtering target power on microstructure and mechanical properties of nanocomposite nc-TiN/a-SiNx thin films, Thin Solid Films 447-448 (2004) 462–467.
[42] Y.C. Chim, X.Z. Ding, X.T. Zeng, S. Zhang, Oxidation resistance of TiN, CrN, TiAlN and CrAlN coatings deposited by lateral rotating cathode arc, Thin Solid Films 517 (2009) 4845–4849.
[43] X. Chen, S. Ma, K. Xu, P.K. Chu, Oxidation behavior of Ti–B–C–N coatings deposited by reactive magnetron sputtering, Vacuum 86 (2012) 1505–1512.
[44] Y. Qin, G. Zheng, L. Zhu, Structure and wear characteristics of TiCN nanocomposite coatings fabricated by reactive plasma spraying, Surface and Coatings Technology 342 (2018) 137–145.